

# Sulfide recrystallization and gold remobilization during the 2.0 Ga stage of the Minas Orogeny: implications for gold mineralization in the Quadrilátero Ferrífero area, Brazil

Mariana Brando Soares<sup>1,2</sup>, David Selby<sup>3,4</sup>, Laurence Robb<sup>5,6</sup>, Atlas Vasconcelos Corrêa Neto<sup>7</sup>

<sup>1</sup>Programa de Pós-Graduação em Geologia (PPGL), Instituto de Geociências, Universidade Federal do Rio de Janeiro, Brazil.

<sup>2</sup>Departamento de Geologia Aplicada, Faculdade de Geologia, Universidade do Estado do Rio de Janeiro, Rio de Janeiro, Brazil

<sup>3</sup>Department of Earth Sciences, Durham University, Durham DH1 3LE, UK

<sup>4</sup>State Key Laboratory of Geological Processes and Mineral Resources, School of Earth Resources, China University of Geosciences, Wuhan, 430074 Hubei, China

<sup>5</sup>Department of Earth Sciences, University of Oxford, Oxford, UK

<sup>6</sup>DSI-NRF Centre of Excellence, University of the Witwatersrand, Johannesburg, RSA

<sup>7</sup>Departamento de Geologia, Instituto de Geociências, Universidade Federal do Rio de Janeiro, Rio de Janeiro, Brazil.

## Abstract

The historical Quadrilátero Ferrífero (QF) mining district in Brazil is a poly-deformed Archean terrane recording several tectonic events. This history has hampered the accurate dating of its important gold deposits given that most of the geochronological clocks have been affected by multiple thermal events. In an attempt to determine an accurate time constraint for the mineralizing events in this region, we provide the first Re-Os dating for a gold deposit in the QF, obtained from 13 mineral separates of disseminated sulfide phases (pyrrhotite, coarse-grained arsenopyrite, fine-grained arsenopyrite, pyrite) at the recently discovered São Sebastião deposit (NW QF). Three distinct successive sulfidation stages are interpreted at the deposit. The final stage, texturally associated with gold, is marked by fine-grained arsenopyrite and pyrite (assemblage III) and is associated with high-temperature (~600°C) features. A Re-Os errorchron is obtained when considering the data of all samples collectively, but a comprehensive Re-Os isochron age of  $1987 \pm 72$  Ma ( $2\sigma$ ;  $n = 4$ ; IsoplotR model 3; initial  $^{187}\text{Os}/^{188}\text{Os} = 2.1 \pm 0.7$ ) is obtained from assemblage III. A  $^{187}\text{Re}$ - $^{187}\text{Os}^r$  isochron at  $1988 \pm 56$  Ma (MSWD = 0.1, initial  $^{187}\text{Os}^r = -0.1 \pm 2.6$  ppt;  $n=4$ ) is obtained if an initial  $^{187}\text{Os}/^{188}\text{Os}$  composition of ca. 2.1, is used, this being consistent with the fact that the  $^{187}\text{Os}$  in the sulfides in assemblage III is largely radiogenic ( $^{187}\text{Os}^r$ ). Earlier assemblages (I and II) individually show variable initial  $^{187}\text{Os}/^{188}\text{Os}$ , indicative of disturbance to the Re-Os systematics at ~2.0 Ga. This age is considered to be the best estimative for the timing of gold mineralization at São Sebastião, being coincident with the waning stages of the Minas Orogeny, the thermal effects of which are restricted to the southern QF. Hence, we consider that the hot fluids from which assemblage III crystallized were responsible for resetting the Re-Os systematics in assemblages I and II, and were central to Paleoproterozoic gold deposition in the region. This ~2.0 Ga age challenges previous notions of a late Archean, ~2.7 Ga, mineralizing event in the QF and makes it possible that gold remobilization occurred elsewhere in the region, particularly in areas representing deeper crustal levels.

## Introduction

The Quadrilátero Ferrífero (QF, **Fig. 1**) area in the southern São Francisco Craton, Brazil, has experienced extensive gold production since the 18<sup>th</sup> century. The superposition of tectonic events in the QF hampers the acquisition and interpretation of absolute isotopic ages of gold mineralization (Lobato et al., 2001b; Lobato et al., 2007). This is further complicated by the presence of different mineralization styles, ages and host-rocks (Renger et al., 1993; Cabral, 1996; Cabral et al., 2001; Lobato et al., 2001 a,b; Koglin et al., 2012; Cabral et al., 2013; Cabral

1  
2  
3  
4  
5  
6  
7  
8  
9  
10  
11  
12  
13  
14  
15  
16  
17  
18  
19  
20  
21  
22  
23  
24  
25  
26  
27  
28  
29  
30  
31  
32  
33  
34  
35  
36  
37  
38  
39  
40  
41  
42  
43  
44  
45  
46  
47  
48 et al., 2015; Tassinari et al., 2015; Brando Soares et al., 2018; Fabricio-Silva, 2019). As a result,  
49 the timing of gold ore formation in the QF is debated. Most of the gold occurrences in this  
50 region, including the world-class Cuiabá and Morro Velho deposits (see location in **Fig. 1**), are  
51 classified as orogenic gold systems and are hosted within the 2.90-2.73 Ga Rio das Velhas  
52 greenstone belt (RVGB - Machado and Carneiro, 1992; Schrank et al., 2002; Hartmann et al.,  
53 2006; Noce et al., 2007; Baltazar and Zucchetti, 2007; Vial et al., 2007; Martins et al., 2016;  
54 Moreira et al., 2016). The aforementioned gold systems are described as being late- to post-  
55 tectonic, slightly postdating the 2.70 - 2.65 Ga peak metamorphism related to the waning stages  
56 of the Rio das Velhas orogenic event (2.8 - 2.75 Ga; Lobato et al. 2001b; 2007; Baltazar and  
57 Zucchetti, 2007; Noce et al., 2007).

58 Various imprecise Pb-Pb model ages for galena, arsenopyrite and pyrite are reported  
59 between 2.7 and 1.9 Ga (Thorpe et al., 1984) for the São Bento and Morro Velho deposits in the  
60 RVGB (see **Fig. 1** for location). These ages are interpreted to reflect the onset of gold deposition  
61 (2.67 - 2.65 Ga), as well as later recrystallization events (2.1-1.9 Ga) (Lobato et al., 2001a). The  
62 younger ages are commonly related to the Minas Orogeny, a 2.47-2.10 Ga Paleoproterozoic  
63 compressive event responsible for arc-amalgamation to the south of the QF during the  
64 Rhyacian-Orosirian (Alkmim and Teixeira, 2017) and correlative with the 2.2 – 2.0 Ga Eburnean  
65 Orogeny in western Africa (McFarlane et al., 2019 and references therein). Similar ages between  
66 2.1 and 1.9 Ga are reported for the Turmalina deposit, located west of the RVGB in the  
67 correlative Pitangui greenstone belt (PGB; **Fig.1**). At Turmalina, these ages are calculated from  
68 Sm-Nd, Rb-Sr and secondary Pb-Pb isotopic studies in garnet, sericite, pyrrhotite and from  
69 arsenopyrite associated with gold mineralization (Tassinari et al., 2015).

70 The first reliable and precise geochronological data for the timing of gold mineralization  
71 in the QF was obtained by U-Pb SHRIMP dating of accessory monazite in association with gold  
72 at the Morro Velho and Cuiabá deposits (Lobato et al., 2007). Data from both deposits yielded  
73 a  $2672 \pm 14$  Ma U-Pb age (Lobato et al., 2007). A further U-Pb SHRIMP ca. 2.7 Ga age ( $2730 \pm 42$   
74 Ma; upper intercept) is reported from hydrothermal monazite within the sulfide-rich zone of  
75 the Lamego deposit, nearby Cuiabá (Martins et al., 2016). Younger U-Pb SHRIMP ages of  $2387$   
76  $\pm 46$  Ga (monazite; upper intercept) and  $518.5 \pm 9$  Ma (xenotime; Concordia age) that are  
77 coincident with the timing of the Minas (2.47-2.1 Ga) and Brasiliano (0.65-0.50 Ga) orogenies,  
78 respectively, are also reported from the Lamego deposit.

79 The rhenium-osmium (Re-Os) isotope system has long been used to date molybdenite,  
80 containing significant concentrations of Re (ppm) and no common Os (Morgan et al., 1968;  
81 Markey et al., 1998; Markey et al., 2007). Improved chemical separation and analytical methods  
82 (Creaser et al., 1991; Shirey and Walker, 1995) have permitted the measurement of Os and Re  
83 at lower concentrations (ppb level Re and ppt level Os) enabling other sulfides (e.g., pyrite,  
84 arsenopyrite, chalcopyrite, bornite, carrollite, cobaltite, löllingite) to be utilized as reliable Re-  
85 Os geochronometers (e.g., Stein et al., 1998b; Stein et al., 2000; Arne et al., 2001; Barra et al.,  
86 2003; Morelli et al., 2005; Feng et al., 2009; Huang et al., 2015; Hnatyshin et al., 2015; Ding et  
87 al., 2016; Saintilan et al., 2017a,b; 2018). Importantly, the Re-Os system allows dating of sulfide  
88 minerals that are directly associated with the ore (e.g., gold), without the need to make  
89 inferences through the dating of other gangue minerals, which may have had a more complex  
90 history (Stein et al., 1998a; Mathur et al., 1999; Morgan et al., 2000; Stein et al., 2000; Arne et  
91 al., 2001).

92 Here, we present here the first direct Re-Os dating for sulfides in the QF to provide an  
93 improved temporal and genetic understanding of gold mineralization in the district. Specifically,  
94 we present Re-Os analyses of pyrrhotite, arsenopyrite, and pyrite from the recently discovered  
95 (2014) São Sebastião gold deposit in the PGB. The Re-Os data permit a discussion regarding the  
96 complex timing and genesis of the gold deposits in this region and helps to provide insights into  
97 the timing and conditions of gold deposition in other areas that record the superposition of  
98 various tectonic events. This is especially relevant in late Archean and Paleoproterozoic terrains,  
99 known globally -as the preferred hosts to- orogenic-gold deposits.

## 100 **Regional Geology**

101 The ca. 3.2 – 2.6 Ga Archean terrane of the QF is composed of TTG-granite complexes  
102 and greenstone belts and records a complex geological history (Lana et al., 2013; Teixeira et al.,  
103 2017; Simon et al., 2018) (**Fig. 1** - Dorr, 1969; Alkmim and Marshak, 1998). This includes; (I) the  
104 Neoproterozoic Rio das Velhas orogenic event (2.80 - 2.75 Ga – Baltazar and Zucchetti, 2007 and  
105 references therein), a progressive regional deformational event dominated by thrust tectonics  
106 ( $D_n + D_{n+1}$ ); (II) the accretionary Paleoproterozoic Minas Orogeny (2.47 - 2.10 Ga; Alkmim and  
107 Teixeira, 2017 and references therein), also known as the Transamazonian event, which has  
108 occurred to the south of the QF and caused the exhumation of TTG-granite domes during the  
109 orogenic collapse, interpreted from a dome-and-keel architecture (Alkmim and Teixeira, 2017;  
110 Cutts et al., 2019); and (III) the Neoproterozoic Brasiliano-Pan African Orogeny (0.65 – 0.50 Ga;

111 e.g., Brito Neves et al., 2014) affecting the E border of the QF close to the Araçuaí (Chemale et  
112 al., 1994; Alkmim and Marshak, 1998) marginal orogenic belt.

113 To date, the gold deposits in the RVGB (the main greenstone belt in the QF) have been  
114 traditionally classified as epi- (150 – 300 °C, < 6 km) to mesozonal (300 – 475 °C, 6 - 12 km)  
115 orogenic-gold systems (Lobato et al., 2001 a,b). The fluids responsible for such mineralization  
116 are described as having originated from metamorphic dehydration at 300 – 350 °C, typical of  
117 many other greenschist-metamorphosed Neoproterozoic terranes (Gebre-Mariam et al., 1995;  
118 Groves et al., 1998; McCuaig and Kerrich, 1998; Jia et al., 2003; Goldfarb and Groves, 2015). In  
119 contrast, the gold deposits in the correlative PGB (**Fig.1**) display high-temperature (500 - 600°C)  
120 features (Brando Soares et al., 2018; Fabricio-Silva et al., 2019) being hosted by rocks  
121 metamorphosed at amphibolite-facies conditions. Such characteristics are typically related with  
122 those of deeper hypozonal (475 – 700 °C, >12 km) gold deposits.

### 123 **Sulfide mineral paragenesis at São Sebastião**

124 São Sebastião is a stratabound, hypozonal gold deposit hosted by 2859 ± 11 Ma banded  
125 iron formation (BIF) layers. The deposit is composed of two main orebodies (Biquinho and  
126 Pimentão) and a satellite body (Tomate) exhibiting a saddle reef-like structure (see **Fig. 2A**).  
127 Gold is contained within sulfide-rich intervals that are spatially associated with  $D_n$  and  $D_{n+1}$  folds  
128 and thrust-related shear zones formed during the NE-SW shortening related to the 2.80 - 2.75  
129 Ga Rio das Velhas orogeny.

130 A recent detailed petrographic study of the sulfide paragenesis identifies at least three  
131 disseminated sulfidation stages at São Sebastião and a late stage of vein formation (Brando  
132 Soares et al., 2018; see **Fig. 2** for main textures and paragenesis). Sulfide assemblage I comprises  
133 disseminated pyrrhotite and chalcopyrite directly associated with structural features related to  
134 an early compressional event (**Fig. 2B, 2C, 2D, 2E**). Sulfide assemblage II is related to coarse-  
135 grained arsenopyrite and rare arsenian pyrite. Coarse-grained arsenopyrite pervasively replaces  
136 assemblage I pyrrhotite (**Fig. 2C, 2D**). Sulfide assemblage III comprises localized fine-grained  
137 arsenopyrite, (As-free) pyrite, quenched Cu-Fe-S intermediate solid solution phase (ISS), plus  
138 minor pyrrhotite and chalcopyrite (**Fig. 2B, 2C, 2F, 2G, 2H, 2I**). The quenched ISS occurs in the  
139 form of irregular pyrrhotite-chalcopyrite intergrown patches only recognized by SEM-EDS (**Fig.**  
140 **2F**). The fine-grained arsenopyrite possibly results from the recrystallization of assemblage II  
141 coarse-grained arsenopyrite (**Fig. 2C, 2G, 2H**). Sulfide assemblage III is restricted to the inner  
142 sections of the ore bodies (see **Fig. 2A**). Gold is found as inclusions in pyrite, filling fractures in

143 pyrite and both coarse- and fine-grained arsenopyrite and in the form of late droplets and  
144 coarser grains at the contact between sulfides and gangue minerals predating vein formation  
145 (**Fig. 2G, 2H, 2I**). The post-ore quartz-sulfide veins contain the youngest generation of pyrite  
146 and chalcopyrite (**Fig. 2E**). Small-scale localized brittle-shearing features are recognized in  
147 association with assemblage III and post-ore veinlets (see **Fig. 2D** at the bottom right corner). A  
148 paragenetic table is available in **Fig. 2J**.

149 Assemblage III is considered to have crystallized from high-temperature (~600°C) Bi-  
150 enriched melts. These were responsible for the destabilization of previous assemblages as well  
151 as the scavenging and re-concentration of gold, and are considered to have had the major  
152 impact on ore formation (see native gold in **Figs. 2G, 2I** and Brando Soares et al., 2018). The  
153 overprint of sulfide paragenesis and its role in ore formation at São Sebastião is also evidenced  
154 by geochemical trends from whole-rock assays. General low to medium gold grades (10 to 6000  
155 ppb) are identified in samples displaying only sulfide assemblage I, where enhanced grades are  
156 associated with increases in S, Ag, Cu and Bi. A second trend is recognized in samples displaying  
157 the sulfide assemblage III overprint exhibiting variable Au grades (60 to 45000 ppb) and  
158 constant high S, Ag, Cu and Bi concentrations. Notably, the highest gold grades (5000 to 45000  
159 ppb) occur in samples where the two geochemical trends and sulfide assemblages overlap,  
160 suggesting a process of gold remobilization and re-concentration triggered by the formation of  
161 sulfide assemblage III.

### 162 **Sampling and methodology**

163 Thirteen sulfide mineral separates were obtained from various drill-core samples from  
164 within the main mineralized section at the São Sebastião deposit (Biquinho body, **Fig.2A**). The  
165 thirteen mineral separates comprise disseminated assemblage I pyrrhotite (n = 4), assemblage  
166 II arsenopyrite (n = 4), and assemblage III arsenopyrite and pyrite (n = 5). Samples # 5 and 10  
167 are composed of mix of very fine-grained (200-500 µm) assemblage III arsenopyrite and pyrite  
168 that could not be separated by the conventional methods described below.

169 The drill core samples (15-20 cm- long) were first crushed in an agate ball mill to prevent  
170 any metal contamination, followed by Frantz magnetic separator, heavy liquids (2.89 g/cm<sup>3</sup>  
171 bromoform) and, finally purified by handpicking using a binocular microscope. For samples #4  
172 #6 and #13, before handpicking, a large amount of fine arsenopyrite not extracted by Frantz  
173 was separated from pyrite of similar grain size by decantation velocity when immersed and  
174 agitated in heavier diiodomethane (3.32 g/cm<sup>3</sup>). This technique was developed for this work

175 and is referred to as the “Wyatt technique”. This method is based on the density contrast  
176 between arsenopyrite ( $6.07 \text{ g/cm}^3$ ) and pyrite ( $5.01 \text{ g/cm}^3$ ). A sample (weighting approximately  
177 1 gram) containing both minerals in a very fine granulometry (200-500  $\mu\text{m}$ ), being very difficult  
178 to handpick, was separated in 4 regular 15 mL test tubes. Each tube was filled with  
179 diiodomethane up to 2 cm from the top. Each mixture in the test tubes was agitated with a glass  
180 rod immediately before the bottom of the tube was rapidly frozen using liquid nitrogen. As a  
181 result, the denser fraction (i.e., arsenopyrite) was concentrated within the frozen bottom after  
182 a few seconds (e.g., 10 s). The light fraction composed mainly of pyrite was washed out of the  
183 tubes using acetone and collected in a filter paper. The denser phase was collected the same  
184 way after the diiodomethane had thawed. The purity of the separates was improved by  
185 handpicking under a light microscope.

186 The sulfide samples were then analyzed at the Source Rock and Sulfide Geochronology  
187 and Geochemistry, and Arthur Holmes Laboratories in the Durham Geochemistry Center at  
188 Durham University, UK, following the procedure described in Selby et al. (2009). Each sample  
189 (~0.4 g) was loaded in a Carius tube with a known amount of mixed  $^{185}\text{Re}$  and  $^{190}\text{Os}$  tracer  
190 solutions and then dissolved and homogenized with a mix of concentrated hydrochloric (3 mL)  
191 and nitric (6 mL) acid at  $220 \text{ }^\circ\text{C}$  for 48 h. The Os was extracted from the acid solution using  
192 solvent extraction ( $\text{CHCl}_3$ ) and purified by microdistillation (Birck et al., 1997). The Re fraction  
193 was isolated using a NaOH-acetone solvent extraction and further purified by standard HCl-  
194  $\text{HNO}_3$  anion-bead exchange chromatography (Selby and Creaser, 2003). The purified Re and Os  
195 fractions were loaded on Ni and Pt filaments, respectively, and analyzed using a Thermo  
196 Scientific Triton thermal ionization mass spectrometer in negative mode (N-TIMS). Total  
197 procedural blanks for Re and Os were  $2.3 \pm 0.2 \text{ pg}$  (picogram) and  $1.00 \pm 0.02 \text{ pg}$ , respectively,  
198 with an average  $^{187}\text{Os}/^{188}\text{Os}$  value of  $0.17 \pm 0.06$  ( $n = 2$ ). Two level absolute uncertainties are  
199 calculated using error propagation and include Re and Os mass spectrometer measurements,  
200 blank abundances and isotopic compositions, spike calibrations, weighing uncertainties of  
201 sample and tracer solution, and reproducibility of standard Re and Os isotope values. The Re-  
202 Os isotopic data including the  $2\sigma$  propagated uncertainties for  $^{187}\text{Re}/^{188}\text{Os}$  and  $^{187}\text{Os}/^{188}\text{Os}$  and  
203 the associated error correlation function ( $\rho$ ) were used to calculate a Re-Os isochron age  
204 using York regression via Isoplot v. 4.15 and IsoplotR with a  $\lambda^{187}\text{Re}$  constant of  $1.666 \times 10^{-11} \text{ yr}^{-1}$   
205 (Smoliar et al., 1996; Ludwig, 2012; Vermeesch, 2018).

## 206 Re-Os geochronology results

207 All Re-Os data for the thirteen samples analyzed are presented in **Table 1** and is also  
208 available as an appendix file (**Appendix Table A1**). Assemblage I pyrrhotite possesses between  
209 ca. 0.24 and 0.98 ppb Re and ca. 18 and 74 ppt Os, and  $^{187}\text{Re}/^{188}\text{Os}$  of ca. 56 to 96 and  $^{187}\text{Os}/^{188}\text{Os}$   
210 of 2.1 to 3.9. In contrast, assemblage II arsenopyrite (Re = 7-14 ppb, Os = 192-416 ppt,  
211  $^{187}\text{Re}/^{188}\text{Os} = 442\text{-}1454$ ,  $^{187}\text{Os}/^{188}\text{Os} = 16.3\text{-}53.2$ ) and assemblage III arsenopyrite/pyrite (Re = 2-  
212 11 ppb, Os = 75-369 ppt,  $^{187}\text{Re}/^{188}\text{Os} = 489\text{-}608$ ,  $^{187}\text{Os}/^{188}\text{Os} = 18.6\text{-}22.6$ ) show considerably  
213 more elevated Re-Os concentrations and isotopic compositions.

214 The absolute timing of mineralization and the temporal duration between assemblages  
215 I, II, III at the São Sebastião deposit is unknown. The relative age of the mineralization from  
216 oldest to youngest based on petrographic observations is assemblage I to III. Firstly, we evaluate  
217 the Re-Os isotope systematics of the entire thirteen samples based on the premise that the  
218 sulfide assemblages are broadly contemporaneous. Collectively the Re-Os isotope data for  
219 assemblage I pyrrhotite, and assemblage II and III arsenopyrite and pyrite scatter about a ca.  
220 2.2 Ga errorchron ( $2151 \pm 86$  Ma;  $2\sigma$ ; MSWD = 375;  $n = 13$ ; York model 3; initial  $^{187}\text{Os}/^{188}\text{Os} =$   
221  $0.08 \pm 0.89$ ; **Fig. 3A**). Given that the sample set represents a number of samples ( $n = 4$  to 5) from  
222 each assemblage (**Table 1; Appendix Table A1**), we consider that this excess data-point scatter  
223 is unlikely to represent an analytical artifact. Instead, the scatter about the best-fit of all the Re-  
224 Os isotope data likely reflect disparate temporally distinct sulfide generations, with, or without,  
225 variable initial  $^{187}\text{Os}/^{188}\text{Os}$  ratios (Osi), and/or disturbance to the Re-Os systematics. These  
226 issues invalidate the isochron dating approach for the entire sample set collectively.

227 Errorchrons are also produced individually for the Re-Os isotope data for assemblage I  
228 ( $1989 \pm 3900$  Ma;  $2\sigma$ ; MSWD = 298;  $n = 4$ ; York model 3; initial  $^{187}\text{Os}/^{188}\text{Os} = 0.1 \pm 5.8$ ; **Fig. 3B**)  
229 and II ( $2187 \pm 340$  Ma;  $2\sigma$ ; MSWD = 224;  $n = 4$ ; York model 3; initial  $^{187}\text{Os}/^{188}\text{Os} = -1.1 \pm 5.3$ ; **Fig.**  
230 **3C**). In contrast, the Re-Os isotope data for assemblage III yield a significantly better linear fit  
231 (MSWD = 31), but still an imprecise age ( $2005 \pm 980$  Ma;  $2\sigma$ ;  $n = 5$ ; York model 3; initial  
232  $^{187}\text{Os}/^{188}\text{Os} = 2.2 \pm 9.0$ ; **Fig. 3D**). For assemblage III, the scatter about the linear best-fit of the  
233 Re-Os data is predominantly controlled by sample #13 that plots above the line of best-fit.  
234 Excluding sample #13, the remaining assemblage III ( $n = 4$ ) Re-Os data yields a Re-Os isochron  
235 age of  $1989 \pm 347$  Ma ( $2\sigma$ ; MSWD = 2.3;  $n = 4$ ; York model 3; initial  $^{187}\text{Os}/^{188}\text{Os} = 2.1 \pm 3.2$ ; **Fig.**  
236 **3d**). To account for the scatter in the Re-Os data, the model 3 approach of Isoplot introduces a  
237 normal distributed variation in the initial  $^{187}\text{Os}/^{188}\text{Os}$  (Ludwig, 2011). In a similar approach to  
238 account for the scatter in the best-fit of the Re-Os data, IsoplotR (Vermeesch, 2018) utilizes a

239 non-normal variation in the initial  $^{187}\text{Os}/^{188}\text{Os}$ , which results in a more precise Re-Os isochron  
age ( $1987 \pm 72$  Ma;  $2\sigma$ ), with a smaller uncertainty in the initial  $^{187}\text{Os}/^{188}\text{Os}$  ( $2.1 \pm 0.7$ ; variation  
in initial  $^{187}\text{Os}/^{188}\text{Os} = 0.00075 + 0.139310 / - 0.000075$  [2s]).

Considering an initial  $^{187}\text{Os}/^{188}\text{Os}$  composition of ca. 2.1 for assemblage III, as given by  
the Re-Os isochron, >89 % of the  $^{187}\text{Os}$  in the assemblage III sulfides is radiogenic ( $^{187}\text{Os}^r$ ) (**Table  
1; Appendix Table A1**). A  $^{187}\text{Re}$ - $^{187}\text{Os}^r$  isochron age for assemblage III, based on  $^{187}\text{Os}^r$  calculated  
using an initial  $^{187}\text{Os}/^{188}\text{Os}$  composition of ca. 2.1 is  $1998 \pm 55$  Ma (2s; Model 1, MSWD = 1.4;  $n$   
= 5; initial  $^{187}\text{Os}^r = 0 \pm 2.6$  ppt), or  $1988 \pm 56$  Ma without sample #13 (Model 1, MSWD = 0.1,  
initial  $^{187}\text{Os}^r = -0.1 \pm 2.6$  ppt; **Fig. 3e**). Collectively, the Re-Os data for assemblage III provide the  
best estimate for the timing of mineralization for this sulfide stage at ca. 2.0 Ga. For the Re-Os  
data of sample #13 to return a ca. 2.0 Ga age, the  $^{187}\text{Os}^r$  must be calculated using an initial  
 $^{187}\text{Os}/^{188}\text{Os}$  of ca. 3, which would explain why sample #13 falls off the best-fit of all other  
assemblage III points on the  $^{187}\text{Re}/^{188}\text{Os}$  vs.  $^{187}\text{Os}/^{188}\text{Os}$  plot (**Fig. 3**).

If it is considered that assemblage II initially formed broadly contemporaneously and  
prior to the 2.0 Ga assemblage III, the scatter about the best-fit of all the assemblage II  
 $^{187}\text{Re}/^{188}\text{Os}$  vs.  $^{187}\text{Os}/^{188}\text{Os}$  data likely reflects disturbance to the Re-Os arsenopyrite systematics  
at ca. 2.0 Ga. This is illustrated by the range of model ages for assemblage II calculated from the  
same initial  $^{187}\text{Os}/^{188}\text{Os}$  composition (**Table 1; Appendix Table A1**). Akin to assemblage III, the  
 $^{187}\text{Os}$  budget of assemblage II is dominated by  $^{187}\text{Os}^r$  (>90 %; **Table 1; Appendix Table A1**).  
Model ages for assemblage II overlap (including uncertainty) with the timing of assemblage III  
(ca. 2.0 Ga) based on  $^{187}\text{Os}^r$  calculated from initial  $^{187}\text{Os}/^{188}\text{Os}$  compositions of 0.12 and 0.5  
(samples #1, 2), 1.0 (samples #1, 2, 3), 1.5 (samples #3, 11) and 2.0 (sample #11) (**Table 1;  
Appendix Table A1**). The latter suggests that the disturbance to the Re-Os isotope systematics  
resulted in the arsenopyrite of assemblage II possessing variable initial  $^{187}\text{Os}/^{188}\text{Os}$  ratios ( $\text{Osi}$ ).  
A similar conclusion of Re-Os isotope disturbance can be made for the assemblage I pyrrhotite.  
Only samples #7 ( $\text{Osi} = 0.5$ ) and #9 ( $\text{Osi} = 0.12$ ) (**Table 1; Appendix Table A1**) return Re-Os model  
ages in line with those given by assemblage III (ca. 2.0 Ga). The remaining samples (#8 and 12)  
all yield ages younger than the 2.0 Ga assemblage III, suggesting that the Re-Os systematics did  
not close at 2.0 Ga, but have been affected by a younger geological event.

## **Discussion and implications for the timing of gold mineralization at São Sebastião**

*Timing relates to Au mineralization and Au upgrading*

270 The Re-Os data for sulfide assemblage III provide the best estimate for the timing of  
271 mineralization at São Sebastião at ca. 2.0 Ga. This age corresponds with the waning stages of  
272 the Minas Orogeny, an accretionary event characterized to the south of the QF in the  
273 allochthonous Mineiro belt (2.47 - 2.10 Ga – Ávila et al., 2010; Teixeira et al., 2015; Alkmim and  
274 Teixeira, 2017). This Paleoproterozoic age is quite distinct from the  $2672 \pm 14$  Ma U-Pb age  
275 obtained for accessory monazites in the Cuiabá and Morro Velho deposits of the RVGB (Lobato  
276 et al., 2007).

277 Certain tectonic features recognized in the QF, such as the Pará de Minas shear zone in  
278 the PGB (**Fig. 1** – Tassinari et al., 2015), are also associated with this time interval (2.1 to 1.9 Ga)  
279 and possibly relate to the gravitational collapse of the Minas orogen (Alkmim and Teixeira,  
280 2017) further to the south. Such structures are interpreted to have reactivated older Archean  
281 crustal discontinuities resulting in a Paleoproterozoic dome-and-keel architecture (Alkmim and  
282 Marshak, 1998; Cutts et al., 2019). This process is driven by means of crustal thinning and uplift  
283 of hot (600 – 700 °C) mid-crustal (20 km) Archean gneiss domes (Alkmim and Marshak, 1998;  
284 Cutts et al., 2019). The thermal effect of this extensional collapse event is reported by regional  
285 resetting of 2100 - 1940 Ma U-Pb ages in titanite and monazite, implying temperatures in the  
286 order of ca. 600–700 °C (Aguilar et al., 2017) at this time. This temperature range is considered  
287 as the minimum closure temperature for such accessory minerals (Scott and St-Onge, 1995),  
288 but is lower than the temperature necessary to disturb/reset the U-Pb systematics of zircon ( $\geq$   
289 700 °C – Lee et al., 1997; Rubatto et al., 2001; Hermann and Rubatto, 2003). The absence of ca.  
290 2.1 Ga U-Pb zircon reset ages in the QF (Romano et al., 2013; Farina et al., 2015; Albert et al.,  
291 2016; Aguilar et al., 2017) supports this temperature constraint.

292 The U-Pb age range in titanite and monazite is very similar to that obtained from the Re-  
293 Os analyses of sulfide assemblage III in this study. Moreover, temperatures around ca. 600 °C,  
294 as implied from the U-Pb systematics and ages of monazite and titanite in the QF (e.g., Aguilar  
295 et al., 2017), are high enough to cause sulfide recrystallization (e.g. Cook et al., 2009) driven by  
296 hydrothermal dissolution and re-precipitation, such as is observed in the São Sebastião gold  
297 deposit. In this regard, the sulfide assemblage III is described to have formed at a similar  
298 temperature (ca. 600 °C) based on the arsenopyrite geothermometer, ISS formation and  
299 crystallization of exotic Bi-sulfosalts of the pavonite group (see Brando Soares et al., 2018). This  
300 further indicates a possible correlation between the formation of assemblage III and the waning  
301 stages of the Minas Orogeny at ca. 2.0 Ga, in a broader regional perspective. As a result, the Re-

1  
2  
3  
4  
5  
6  
7  
8  
9  
10  
11  
12  
13  
14  
15  
16  
17  
18  
19  
20  
21  
22  
23  
24  
25  
26  
27  
28  
29  
30  
31  
32  
33  
34  
35  
36  
37  
38  
39  
40  
41  
42  
43  
44  
45  
46  
47  
48  
49  
50  
51  
52  
53  
54  
55  
56  
57  
58  
59  
60  
61  
62  
63  
64  
65

302 Os systematics of the early sulfide assemblages (I and II) at São Sebastião may have been reset  
303 by higher-temperature fluid fluxes at 2.0 Ga. This being also coeval (within uncertainty) with  
304 the sulfide recrystallization evident in assemblage III. For instance, the Re-Os system in  
305 arsenopyrite has been shown to be preserved up to temperatures as high as 400 °C, and  
306 possibly exceeding 450 °C (Morelli et al., 2010), but is expected to be reset at higher  
307 temperatures.

308 The highest gold grades at São Sebastião, which are associated with assemblage III, were  
309 developed preferentially in sites where gold was re-concentrated/upgraded from sulfide  
310 assemblages (I) and (II). This is shown both by petrography and by two distinct whole-rock  
311 geochemical trends (see **Section 2**). Thus, gold remobilization at São Sebastião is associated  
312 with the high-T recrystallization of sulfides at ca. 2.0 Ga, yielding assemblage III comprising  
313 mainly fine-grained arsenopyrite and pyrite. This sulfide recrystallization stage is accompanied  
314 by infills of native gold and native bismuth in fractures of arsenopyrite (both coarse- and fine-  
315 grained) and pyrite, where Au and Bi remained in the liquid phase until the low cooling  
316 temperature of 271°C (Brando Soares et al., 2018). Since gold fills fractures in recrystallized  
317 sulfides, we propose that the final crystallization of native gold slightly postdates these phases.

318 Overall, the timing for gold mineralization proposed in this study (ca. 2.0 Ga) is  
319 consistent, in part, with the proposals of Tassinari et al. (2015). They advocated a ca. 2.0 Ga  
320 sulfidation and gold-mineralizing stage at the Turmalina deposit, near to São Sebastião.  
321 However, remobilization from a previous Archean assemblage was not considered. Here, gold  
322 remobilization from a Neoproterozoic sulfide-rich paragenesis triggered by sulfide recrystallization  
323 is proposed, similar to that described in the Western Churchill Province, Canada (Lawley et al.,  
324 2015). This is supported by petrographic observations and whole-rock geochemistry indicating  
325 Au-enrichment in zones of overprinted sulfide assemblages, as well as contrasting initial  
326  $^{187}\text{Os}/^{188}\text{Os}$  (Osi) ratios between the early and late sulfide subsets marking the reset of the Re-  
327 Os isotopic clock in the earlier paragenetic sequences. Given that the sulfide recrystallization  
328 likely occurred during Paleoproterozoic times, gold remobilization is assumed to be of the same  
329 age. Moreover, at São Sebastião, we emphasize that the hypozonal features of the  
330 mineralization were attained during at ca. 2.0 Ga at ca. 600 °C, which is equivalent with depths  
331 of > 12 km and amphibolite-facies metamorphic conditions. This is typical of deeply-emplaced  
332 gold deposits where the overprints of a late, high-temperature assemblage are usually

333 associated with gold deposition that is either syn- or post-metamorphic (see Bouchot et al.,  
334 2005; Tomkins et al., 2006; Tomkins et al., 2007, Hagemann et al., 2013 and Kolb et al., 2015).

335 The São Sebastião sulfide assemblage III is here estimated to have formed at  
336 amphibolite-facies conditions during the waning stages of the Minas Orogeny. This, however,  
337 requires that the effects of this tectono-thermal event are more widespread than considered  
338 in previous literature (Alkmim and Teixeira, 2017). The findings in the present work can be  
339 combined with the ca. 2.0 Ga titanite resetting ages reported in the PGB area (Aguilar et al.,  
340 2017) to propose an extension of the thermal imprint area of the Minas Orogeny. The actual  
341 imprint front is likely to be located approximately 100 km NW from where the 2.1 Ga  
342 convergent structures and rocks are recognized (limit between the autochthonous and  
343 allochthonous Mineiro Belt in **Fig. 1**).

344 As such, we speculate that the wider thermal effect of the Minas Orogeny is related to  
345 deep extensional features caused by the collapse of the Paleoproterozoic orogen (e.g., Aguilar  
346 et al. (2017), Alkmim and Teixeira (2017) and Cutts et al. (2019). The high-temperature  
347 assemblages imply that the gold deposits in the PGB (São Sebastião, Turmalina) formed at a  
348 deeper crustal level compared to the deposits in the RVGB (e.g., world-class Cuiabá), which  
349 show epi- to mesozonal characteristics). It is possible, however, that high-T sulfide  
350 remobilization also played a role deeper in the RVGB based on ca. 2.1 Ga resetting ages reported  
351 for this area at Lamego (Martins et al., 2016). In this sense, further investigation by Re-Os  
352 geochronology may provide important insights on the evolution of gold deposits in the south  
353 São Francisco Craton, where the reactivation of Archean NW-SE structures may have had an  
354 important role in transporting fluids from younger hydrated sources. Remarkably, ca. 2.0 Ga  
355 ages are often reported for gold deposits in the West Africa Craton (e.g., Mignot et al., 2017),  
356 but have seldom been described in the correlative São Francisco Craton. Dating mineralization  
357 events may, therefore, be an important tool to more comprehensively understand the  
358 reworking of Archean gold deposits in Brazil and to improve exploration models for similar  
359 multistage ore deposits occurring elsewhere in poly-deformed terranes.

## 360 **Conclusions**

361 At the hypozonal São Sebastião gold deposit (Pitangui greenstone belt) in the QF mining  
362 district in Brazil, gold is associated with sulfide-rich layers within Archean BIF. Rhenium-osmium  
363 geochronometry of the paragenetically youngest sulfide assemblage III provides the best  
364 estimate for the timing (ca. 2.0 Ga) of sulfide and gold mineralization at São Sebastião. This age

365 coincides with the waning stages of the Minas Orogeny. The ca. 2.0 Ga age is different to the  
366 ages reported for other gold deposits in the nearby Rio das Velhas greenstone belt (ca. 2.7 Ga),  
367 but is identical to U-Pb ages obtained previously for titanite and monazite in the QF that are  
368 attributed to record the timing of resetting of the mineral U-Pb systematics. This resetting is  
369 related to the thermal effects (ca. 600°C) of extensional features resulted to the collapse of a  
370 Paleoproterozoic accretionary orogen (Mineiro Belt) known approximately 100 km to the south  
371 of São Sebastião. Thus, the late sulfidation stage (assemblage III) at São Sebastião is considered  
372 to have formed by recrystallization of the earlier sulfide assemblages, which had their Re-Os  
373 systematic reset at ca. 2.0 Ga. Gold is mostly observed filling fractures in arsenopyrite and pyrite  
374 and in the form of late droplets and crystals displaying an association with Bi. In addition, the  
375 highest gold grades are seen in zones where the early and late sulfide paragenesis overlap. This  
376 implies that gold was probably remobilized from the early paragenetic sequence and re-  
377 concentrated by the high-T sulfide association in Paleoproterozoic times. The regional  
378 implications are that the overprinting thermo-tectonic effects of the Paleoproterozoic (2.47 -  
379 2.10 Ga) Minas Orogeny can be traced much further north than previously known. This suggests  
380 that important gold occurrences in the neighboring Rio das Velhas greenstone belt, such as the  
381 world-class Cuiabá deposit, may also have been regenerated at this time. This is supported by  
382 the ca. 2.1 Ga U-Pb age for monazite from the meso- to epizonal sections of these deposits. In  
383 turn, this implies that yet undiscovered hypozonal deposits may exist in the RVGB, beneath the  
384 currently explored depths. In more general terms it is possible that Paleoproterozoic rocks may  
385 represent important targets for gold mineralization in the QF, and indeed the broader São  
386 Francisco craton and its correlatives worldwide.

### 387 **Acknowledgements**

388 This work would not be possible without the support and materials provided by  
389 IAMGOLD Brazil. The results and discussions are part of the PhD thesis of M. Brando Soares  
390 (CNPq 142210/2016-1 and FAPERJ TEC-Nota 10 – E-26/200.281/2017 – 230521 grants). DS  
391 acknowledges the Total Endowment Fund and the CUG Wuhan Dida Scholarship. M. Brando  
392 Soares also thanks Owen Green, and especially chemist Steve Wyatt, for helping with the Re-  
393 Os sample preparation and development of density decantation with liquid nitrogen technique  
394 for mineral separation, here referred to as the “Wyatt technique”.

### 395 **References**

- 396 Aguilar, C., Alkmim, F.F., Lana, C., Farina, F., 2017. Palaeoproterozoic assembly of the São  
1 397 Francisco craton, SE Brazil: New insights from U–Pb titanite and monazite dating. *Precambrian*  
2 398 *Res.* 289, 95-115.  
3  
4  
5 399 Albert, C., Farina, F., Lana, C., Stevens, G., Storey, C., Gerdes, A., Dopico, C.M., 2016. Archean  
6 400 crustal evolution in the Southern São Francisco craton, Brazil: Constraints from U-Pb, Lu-Hf and  
7 401 O isotope analyses. *Lithos* 266-267; 64-86.  
8  
9  
10 402 Alkmim, F.F., Marshak, S., 1998. Transamazonian Orogeny in the Southern São Francisco Craton,  
11 403 Minas Gerais, Brazil: evidence for Paleoproterozoic collision and collapse in the Quadrilátero  
12 404 Ferrífero. *Precambrian Research* 90, 29–58.  
13  
14  
15 405 Alkmim, F.F., Teixeira, W., 2017. The Paleoproterozoic Mineiro Belt and the Quadrilátero  
16 406 Ferrífero. pp. 71–94.  
17  
18 407 Arne, D.C., Bierlin, F.P., Morgan, J.W., Stein, H.J., 2001. Re-Os dating of sulfides associated with  
19 408 gold mineralization in Central Victoria, Australia. *Econ. Geol.* 96, 1455–1459.  
20  
21  
22 409 Ávila, C.A., Teixeira, W., Cordani, U.G., Moura, C.A.V., Pereira, R.M., 2010. Rhyacian (2.23–2.20  
23 410 Ga) juvenile accretion in the southern São Francisco craton, Brazil: geochemical and isotopic  
24 411 evidence from the Serrinha magmatic suite, Mineirobelt. *J. S. Am. Earth Sci.* 29, 464–482.  
25  
26 412 Baltazar, O.F., Zucchetti, M., 2007. Lithofacies associations and structural evolution of the  
27 413 Archean Rio das Velhas greenstone belt, Quadrilátero Ferrífero, Brazil: a review of the regional  
28 414 setting of gold deposits. *Ore Geology Reviews* 32, 471–499.  
29  
30  
31 415 Barra, F., Ruiz, J., Mathur, R., Titley, S., 2003. A Re-Os study of sulfide minerals from the Bagdad  
32 416 porphyry Cu-Mo deposit, northern Arizona, USA. *Miner. Depos.* 38, 585–596.  
33  
34  
35 417 Birck, J.L., RoyBarman, M., Capmas, F., 1997. Re-Os measurements at the femtomole level in  
36 418 natural samples. *Geostand. Newslett.* 20, 19–27.  
37 419  
38  
39 420 Bouchot, V., Ledru, P., Lerouge, C., Lescuyer, J., Milesi, J., 2005. Late Variscan mineralizing  
40 421 systems related to orogenic processes: The French Massif Central. *Ore Geology Reviews* 27,  
41 422 169-197.  
42  
43  
44 423 Brando Soares, M., Corrêa Neto, A.V., Bertolino, L. C., Alves, F.E.A., Almeida, A.M., Silva, P.H.M.,  
45 424 Araújo, R.O., Manduca, L.G., Araújo, I.M.C.P., 2018. Multistage Mineralization at the Hypozonal  
46 425 São Sebastião Gold Deposit, Pitangui Greenstone Belt, Minas Gerais, Brazil. *Ore Geology*  
47 426 *Reviews* 102, 618-638.  
48  
49  
50 427 Brito Neves, B.B., Fuck, R.A., Pimentel, M.M., 2014. The Brasiliano collage in South America: a  
51 428 review. *Brazilian Journal of Geology* 44 (3), 493-518.  
52  
53  
54 429 Cabral, A.R., 1996. Mineralização de ouro paladiado em itabiritos: a jacutinga de Gongo Soco,  
55 430 Quadrilátero Ferrífero, Minas Gerais. MSc thesis, Universidade Estadual de Campinas,  
56 431 Campinas, Brazil.  
57  
58  
59  
60  
61  
62  
63  
64  
65

432 Cabral, A.R., Lehmann, B., Kwitko, R., Jones, R.D., Pires, F.R.M., Filho, O.G.R., Innocentini, M.D.,  
1 433 2001. Palladium-oxygenated compounds of the Gongo Soco mine, Quadrilátero Ferrífero,  
2 434 central Minas Gerais, Brazil. *Mineral. Mag.* 65, 169-179  
3  
4  
5 435 Cabral, A.R., Koglin, N., Strauss, H., Brätz, H., Kwitko-Ribeiro, R., 2013. Regional sulfate-  
6 436 hematite-sulfide zoning in the auriferous Mariana anticline, Quadrilátero Ferrífero of Minas  
7 437 Gerais, Brazil. *Miner. Depos.* 48, 805–816.  
8  
9  
10 438 Cabral, A.R. & Zeh, A., 2015. Detrital zircon without detritus: a result of 496-Ma-old fluid–rock  
11 439 interaction during the gold-lode formation of Passagem, Minas Gerais, Brazil. *Lithos* 212–215,  
12 440 415–427.  
13  
14 441  
15 442 Chemale Jr., F., Rosière, C.A., Issamu, E., 1994. The tectonic evolution of the Quadrilátero  
16 443 Ferrífero, Minas Gerais, Brazil. *Precambrian Research* 65, 25-54.  
17  
18  
19 444 Cook, N.J., Ciobanu, C.L., Mao, J., 2009. Textural control on gold distribution in As-free pyrite  
20 445 from the Dongping, Huangtuliang and Hougou gold deposits, North China Craton (Hebei  
21 446 Province, China). *Chem. Geol.* 264, 101–121.  
22  
23  
24 447 Creaser, R.A., Papanastassiou, D.A., Wasserburg, G.J., 1991. Negative thermal ion mass  
25 448 spectrometry of osmium, rhenium and iridium. *Geochim. Cosmochim. Acta* 55, 397–401.  
26  
27  
28 449 Cutts, K., Lana, C., Alkmim, F., Farina, F., Moreira, H., Coelho, V., 2019. Metamorphism and  
29 450 exhumation of basement gneiss domes in the Quadrilátero Ferrífero: Two stage dome-and-keel  
30 451 evolution? *Geosci. Front.*10 (5), 1765-1787.  
31  
32  
33 452 Ding, C., Nie, F., Bagas, L., Dai, P., Jiang, S., Ding, C., Liu, C., Peng, Y., Zhang, G., Shao, G., 2016.  
34 453 Pyrite Re-Os and zircon U-Pb dating of the Tugurige gold deposit in the western part of the  
35 454 Xing’an-Mongolia Orogenic Belt, China and its geological significance. *Ore Geol. Rev.* 72, 669–  
36 455 681.  
37  
38  
39 456 Dorr, J.V.N.II, 1969. Physiographic, stratigraphic and structural development of the Quadrilátero  
40 457 Ferrífero, Minas Gerais, Brazil. *USGS Professional Paper* 641-A, p. 110.  
41  
42  
43 458 Fabricio-Silva, W., Rosière, C.A., Bühn, B., 2019. The shear zone-related gold mineralization at  
44 459 the Turmalina deposit, Quadrilátero Ferrífero, Brazil: structural evolution and the two stages of  
45 460 mineralization. *Mineralium Deposita* 54, 347-368.  
46  
47  
48 461 Farina, F., Albert, C., Lana, C., 2015. The Neoproterozoic transition between medium- and high-K  
49 462 granitoids: Clues from the Southern São Francisco Craton (Brazil). *Precambrian Res.* 266, 375–  
50 463 394.  
51  
52  
53 464 Feng, C.Y., Qu, W.J., Zhang, D.Q., Dang, X.Y., Du, A.D., Li, D.X., She, H.Q., 2009. Re–Os dating of  
54 465 pyrite from the Tuolugou stratabound Co (Au) deposit, eastern Kunlun Orogenic Belt,  
55 466 northwestern China. *Ore Geol. Rev.* 36 (1), 213–220.  
56  
57 467  
58 468 Gebre-Mariam, M., Hagemann, S.G., Groves, D.I., 1995. A classification scheme for epigenetic  
59 469 Archaean lode-gold deposits. *Miner. Depos.* 30 (5), 408-410.  
60  
61  
62  
63  
64  
65

470

- 1 471 Goldfarb, R.J. and Groves, D.I., 2015. Orogenic gold: Common or evolving fluid and metal  
2 472 sources through time. *Lithos* 233, 2-26.
- 3  
4  
5 473 Groves, D.I., Goldfarb, R.J., Gebre-Mariam, M., Hagemann, S.G., Robert, F., 1998. Orogenic gold  
6 474 deposits: a proposed classification in the context of their crustal distribution and relationship  
7 475 to other gold deposit types. *Ore Geology Reviews* 13 (1-5), 7-27.
- 8  
9  
10 476 Groves, D. I., Santosh, M., Deng, J., Wang, Q., Yang, L., & Zhang, L. (2020). A holistic model for  
11 477 the origin of orogenic gold deposits and its implications for exploration. *Mineralium Deposita*,  
12 478 55(2), 275–292.
- 13  
14  
15 479 Hagemann, S. G., Cassidy, K., Witt., W., 2013. Gold Systems in the Lower Crustal Section  
16 480 (“bottom”) of Greenstone Belts. 12th SGA Biennial Meeting 2013. Proceedings, Volume 3.
- 17 481  
18 482 Hartmann, L.A., Endo, I., Suita, M.T.F., Santos, J.O.S., Frantz, J.C., Carneiro, M.A., McNaughton,  
19 483 N.J., Barley, M.E., 2006. Provenance and age delimitation of Quadrilátero Ferrífero sandstones  
20 484 based on zircon U-Pb isotopes. *Journal of South American Earth Sciences* 20, 273–285.
- 21 485  
22 486 Hermann, J., Rubatto, D., 2003. Relating zircon and monazite domains to garnet growth zones:  
23 487 Age and duration of granulite facies metamorphism in the Val Malenco lower crust. *J.*  
24 488 *Metamorph. Geol.* 21, 833–852.
- 25  
26  
27  
28  
29 489 Hnatyshin, D., Creaser, R.A., Wilkinson, J.J., Gleeson, S.A., 2015. Re-Os dating of pyrite confirms  
30 490 an early diagenetic onset and extended duration of mineralization in the Irish Zn-Pb ore field.  
31 491 *Geology* 43, 143–146.
- 32  
33  
34 492 Huang, X.W., Gao, J.F., Qi, L., Zhou, M.F., 2015. In-situ LA-ICP-MS trace elemental analyses  
35 493 of magnetite and Re–Os dating of pyrite: the Tianhu hydrothermally remobilized sedimentary  
36 494 Fe deposit, NW China. *Ore Geol. Rev.* 65, 900–916.
- 37 495  
38 496 Jia, Y., Kerrich, R., Goldfarb, R., 2003. Metamorphic Origin of Ore-Forming Fluids for Orogenic  
39 497 Gold-Bearing Quartz Vein Systems in the North American Cordillera: Constraints from a  
40 498 Reconnaissance Study of  $\delta^{15}\text{N}$ ,  $\delta\text{D}$ , and  $\delta^{18}\text{O}$ . *Economic Geology* 98, 109-123.
- 41  
42  
43  
44 499 Koglin, N., Cabral, A.R., Brunetto, W.J., Vymazalová, A., 2012. Gold–tourmaline assemblage in a  
45 500 Witwatersrand-like gold deposit, Ouro Fino, Quadrilátero Ferrífero of Minas Gerais, Brazil: the  
46 501 composition of gold and metallogenic implications. *Neues Jahrb. für Mineral. - Abhandlungen*  
47 502 *J. Mineral. Geochemistry* 189, 263–273
- 48  
49  
50  
51 503 Kolb, J., Dziggel, A., Bagas, L., 2015. Hypozonal lode gold deposits: A genetic concept based on  
52 504 a review of the New Consort, Renco, Hutti, Hira Buddini, Navachab, Nevoria and The Granites  
53 505 deposits. *Precambrian Research* 262, 20-44.
- 54  
55  
56 506 Lana, C., Alkmim, F.F., Armstrong, R., Scholz, R., Romano, R., Nalini, H.A., 2013. The ancestry  
57 507 and magmatic evolution of Archean TTG rocks of the Quadrilátero Ferrífero province, southeast  
58 508 Brazil. *Precambrian Research* 230, 1-30.
- 59  
60  
61  
62  
63  
64  
65

- 509 Lawley, C.J.M., Creaser, R.A., Jackson, S.E., Yang, Z., Davis, B.J., Pehrsson, S.J., Dubé, B., Mercier-  
1 510 Langevin, P., Vaillancourt, D., 2015. Unraveling the Western Churchill Province Paleoproterozoic  
2 511 Gold Metallotect: Constraints from Re-Os Arsenopyrite and U-Pb Xenotime Geochronology and  
3 512 LA-ICP-MS Arsenopyrite Trace Element Chemistry at the BIF-Hosted Meliadine Gold District,  
4 513 Nunavut, Canada. *Econ. Geol.* 110, 1425–1454.  
5  
6  
7 514 Le Mignot, E., Reisberg, L., André-Mayer, A.S., Bourassa, Y., Fontaine, A., Miller, J., 2017. Re-Os  
8 515 geochronological evidence for multiple Paleoproterozoic gold events at the scale of the West  
9 516 African craton. *Econ. Geol.* 112, 145–168.  
10  
11  
12 517 Lee, J.K.W., Williams, I.S., Ellis, D.J., 1997. Pb, U and Th diffusion in natural zircon. *Nature* 390,  
13 518 159-161.  
14  
15  
16 519 Lobato, L.M., Ribeiro-Rodrigues, L.C., Zucchetti, M., Noce, C.M., Baltazar, O.F., Silva, L.C., Pinto,  
17 520 C.P., 2001a. Brazil's premier gold province. Part I: The tectonic, magmatic and structural setting  
18 521 of Archean Rio das Velhas greenstone belt, Quadrilátero Ferrífero. *Mineralium Deposita* 36,  
19 522 228–248.  
20  
21  
22 523 Lobato, L.M., Rorigues, L.C.R., Vieira, F.W.V., 2001b. Brazil's premier gold province. Part II:  
23 524 geology and genesis of gold deposits in the Archean Rio das Velhas greenstone belt,  
24 525 Quadrilátero Ferrífero. *Mineralium Deposita* 36, 249–277.  
25  
26  
27 526 Lobato, L.M., Santos, J.O.S., McNaughton, N.J., Fletcher, I.R., Noce, C.M., 2007. U-Pb SHRIMP  
28 527 monazite ages of the giant Morro Velho and Cuiabá gold deposits, Rio das Velhas greenstone  
29 528 belt, Quadrilátero Ferrífero, Minas Gerais, Brazil. *Ore Geology Reviews* 32, 674-680.  
30  
31  
32 529 Ludwig, K., 2012. User's Manual for Isoplot 3.75: A Geochronological Tool for Microsoft Excel.  
33 530 Berkeley Geochronol. Cent. Spec. Publ. No. 5.  
34  
35  
36 531 Machado, N., and Carneiro, M.A., 1992. U-Pb evidence of late Archean tectono-thermal activity  
37 532 in the southern São Francisco shield, Brazil. *Canadian Journal of Earth Sciences*. 29 (11), 2341-  
38 533 2346.  
39  
40 534  
41 535 Markey, R., Stein, H., and Morgan, J., 1998, Highly precise Re-Os dating for molybdenite using  
42 536 alkaline fusion and NTIMS: *Talanta*, v. 45, p. 935–946.  
43  
44 537  
45 538 Markey, R., Stein, H.J., Hannah, J.L., Zimmerman, A., Selby, D., and Creaser, R.A., 2007,  
46 539 Standardizing Re-Os geochronology: A new molybdenite reference material (Henderson, USA)  
47 540 and the stoichiometry of Os salts: *Chemical Geology*, v. 244, p. 74–87.  
48  
49 541  
50 542 Martins, B.S., Lobato, L.M., Rosière, C.A., Hagemann, S.G., Santos, J.O., Villanova, F.L., Silva, R.C.,  
51 543 Lemos, L.H., 2016. The Archean BIF-hosted Lamego gold deposit, Rio das Velhas greenstone  
52 544 belt, Quadrilátero Ferrífero: Evidence for Cambrian structural modification of an Archean  
53 545 orogenic gold deposit. *Ore Geology Reviews* 72, 963-988.  
54  
55  
56 546 Mathur, R., Ruiz, J., Tornos, F., 1999. Age and sources of the ore at Tharsis and Rio Tinto, Iberian  
57 547 pyrite belt, from Re–Os isotopes. *Mineral. Deposita* 34, 790–793.  
58  
59 548  
60  
61  
62  
63  
64  
65

- 1 549 McCuaig, C., Kerrich, R., 1998. P-T-t-deformation-fluid characteristics of lode gold deposits:  
2 550 Evidence from alteration systematics. *Ore Geology Reviews* 12, 381-453.
- 3  
4 551 McFarlane, H.B., Ailleres, L., Betts, P., Ganne, J., Baratoux, L., Jessell, M.W., Block, S., 2019.  
5 552 Episodic collisional orogenesis and lower crust exhumation during the Palaeoproterozoic  
6 553 Eburnean Orogeny: Evidence from the Sefwi Greenstone Belt, West African Craton.  
7 554 *Precambrian Res.* 325, 88–110.
- 8  
9  
10 555 Mitrofanov, A., Cole, G., 2020. Independent Technical Report for the São Sebastião Gold  
11 556 Deposit, Pitangui Gold Project, Brazil. SRK Consulting. 113p.
- 12  
13  
14 557 Moreira, H., Lana, C., Nalini, H.A., 2016. The detrital zircon record of an Archaean convergent  
15 558 basin in the southern São Francisco craton, Brazil. *Precambrian Research* 275, 84-99.
- 16  
17 559 Morelli R.M., Creaser R.A., Selby D., Kontak D.J., Horne R.J., 2005. Rhenium–osmium  
18 560 geochronology of arsenopyrite in Meguma Group gold deposits, Meguma Terrane, Nova Scotia,  
19 561 Canada: evidence for multiple gold-mineralizing events. *Econ Geol* 100:1229–1242.
- 20 562  
21 563 Morgan, J.W., Lovering, J.F., and Ford, R.J., 1968, Rhenium and non-radiogenic osmium in  
22 564 Australian molybdenites and other sulphide minerals by neutron activation analysis. *Journal of*  
23 565 *the Geological Society of Australia*, 15, 189–194.
- 24 566  
25 567 Morgan J.W., Stein H.J., Hannah J.L., Markey R.J., and Wiszniewska J., 2000. Re–Os study of  
26 568 ores from the Suwalki Anorthosite massif, northeast Poland. *Mineralium Deposita* 35: 391–401.
- 27 569  
28 570 Noce, C.M., Tassinari, C., Lobato, L.M., 2007. Geochronological framework of the Quadrilátero  
29 571 Ferrífero, with emphasis on the age of gold mineralization hosted in Archean greenstone belts.  
30 572 *Ore Geology Reviews* 32, 500–510.
- 31 573  
32 574 Renger., F., Suckau, V., Silva, R.M.P., 1993. Sedimentologia e análise da bacia da Formação  
33 575 Moeda, Quadrilátero Ferrífero, Minas Gerais, Brasil. In: SIMPÓSIO DE GEOLOGIA DE MINAS  
34 576 GERAIS, 7., 23-26 nov. 1993, Belo Horizonte, p. 41-45.
- 35 577  
36 578 Romano, R., Lana, C., Alkmim, F.F., Stevens, G., Armstrong, R., 2013. Stabilization of the  
37 579 southern portion of the São Francisco craton, SE Brazil, through a long-lived period of potassic  
38 580 magmatism. *Precambrian Research* 224, 143–159.
- 39 581  
40 582 Rubatto, D., Williams, I.S., Buick, I.S., 2001. Zircon and monazite response to prograde  
41 583 metamorphism in the Reynolds Range, central Australia. *Contrib. Miner. Petrol.* 140, 458–468.
- 42 584  
43 585 Saintilan, N.J., Creaser, R.A., Spry, P.G., Hnatyshin, D., 2017a. Re-Os Systematics of löllingite and  
44 586 arsenopyrite in granulite-facies garnet rocks: Insights into the metamorphic history and thermal  
45 587 evolution of the broken hill block during the early mesoproterozoic (New South Wales,  
46 588 Australia). *Can. Mineral.* 55, 29–44.
- 47 589  
48 590 Saintilan, N.J., Creaser, R.A., Bookstrom, A.A., 2017b. Re-Os systematics and geochemistry of  
49 591 cobaltite (CoAsS) in the Idaho cobalt belt, Belt-Purcell Basin, USA: Evidence for middle  
50  
51  
52  
53  
54  
55  
56  
57  
58  
59  
60  
61  
62  
63  
64  
65

- 1 591 Mesoproterozoic sediment-hosted Co-Cu sulfide mineralization with Grenvillian and  
2 592 Cretaceous remobilization. *Ore Geol. Rev.* 86, 509–525.
- 3  
4 593 Saintilan, N.J., Selby, D., Creaser, R.A., Dewaele, S., 2018. Sulphide Re-Os geochronology links  
5 594 orogenesis, salt and Cu-Co ores in the Central African Copperbelt. *Sci. Rep.* 8.
- 6  
7 595 Schrank, A., Machado, N., Stern, R., 2002. Eventos no Arqueano com base em idades U/Pb–  
8 596 SHRIMP de zircões detríticos em metassedimentos da mina de Morro Velho–Quadrilátero  
9 597 Ferrífero–Minas Gerais. 41th Congresso Brasileiro de Geologia, Sociedade Brasileira de  
10 598 Geologia, João Pessoa, p. 527.
- 11  
12  
13 599 Scott, D.J., St-Onge, M.R., 1995. Constraints on Pb closure temperature in titanite based on  
14 600 rocks from the Ungava orogen, Canada: implications for U-Pb geochronology and P-T-t path  
15 601 determinations. *Geology* 23, 1123–1126.
- 16  
17  
18 602 Selby, D., Creaser, R.A., 2003. Re-Os geochronology of organic rich sediments: An evaluation of  
19 603 organic matter analysis methods. *Chem. Geol.* 200, 225–240.
- 20  
21  
22 604 Selby, D., Kelley, K.D., Hitzman, M.W., Zieg, J., 2009. Re-Os sulfide (bornite, chalcopyrite and  
23 605 pyrite) systematics of the carbonate-hosted copper deposits at Ruby Creek, southern Brooks  
24 606 Range, Alaska. *Econ. Geol.* 104, 437–444.
- 25  
26  
27 607 Shirey, S.B., Walker, R.J., 1995. Carius Tube Digestion for Low-Blank Rhenium-Osmium Analysis.  
28 608 *Anal. Chem.* 67, 2136–2141.
- 29  
30  
31 609 Simon, M.B., Marques Bongiolo, E., Ávila, C.A., Oliveira, E.P., Teixeira, W., Stohler, R.C., Soares  
32 610 de Oliveira, F.V., 2018. Neoproterozoic reworking of TTG-like crust in the southernmost portion of  
33 611 the São Francisco Craton: U-Pb zircon dating and geochemical evidence from the São Tiago  
34 612 Batholith. *Precambrian Res.* 314, 353–376.
- 35  
36  
37 613 Smoliar, M.I., Walker, R.J., Morgan, J.W., 1996. Re-Os ages of group IIA, IIIA, IVA, and IVB iron  
38 614 meteorites. *Science* 271, 1099–1102.
- 39  
40  
41 615 Stein, H.J., Morgan, J.W., Markey, R.J., and Hannah, J.L., 1998a, An introduction to Re-Os:  
42 616 What’s in it for the mineral industry?: *SEG Newsletter*, January 1998, no. 32, p. 1, 8–15.
- 43  
44  
45 617 Stein, H.J., Sundblad, K., Markey, R.J., Morgan, J.W., and Motuza, G., 1998b, Re-Os ages for  
46 618 Archaean molybdenite and pyrite, Kuittila-Kivisuo, Finland and Proterozoic molybdenite,  
47 619 Kabeliai, Lithuania: Testing the chronometer in a metamorphic and metasomatic setting:  
48 620 *Mineralium Deposita*, v. 33, p. 329–345.
- 49  
50  
51 621 Stein, H.J., Morgan, J.W., Scherstén, A., 2000. Re-os Dating of Low-Level Highly Radiogenic  
52 622 (LLHR) Sulfides: the Harnäs Gold Deposit, Southwest Sweden, Records Continental-Scale  
53 623 Tectonic Events. *Econ. Geol.* 95, 1657–1672.
- 54  
55  
56 624 Tassinari, C.C.G., Mateus, A.M., Velásquez, M.E., Munhá, J.M.U., Lobato, L.M., Bello, R.M.,  
57 625 Chiquini, A.P., Campos, W.F., 2015. Geochronology and thermochronology of gold  
58 626  
59 627  
60 628  
61  
62  
63  
64  
65

631 mineralization in the Turmalina deposit, NE of the Quadrilátero Ferrífero Region, Brazil. *Ore*  
632 *Geology Reviews* 67, 368-381.

633 Teixeira, W., Ávila, C.A., Dussin, I.A., Corrêa Neto, A.V., Bongioiolo, E.M., Santos, J.O., Barbosa,  
634 N.S., 2015. A juvenile accretion episode (2.35–2.32 Ga) in the Mineiro belt and its role to the  
635 Minas accretionary orogeny: zircon U-Pb–Hf and geochemical evidences. *Precambrian Research*  
636 256, 148–169.

637 Teixeira, W., Oliveira, E.P., Marques, L.S., 2017. Nature and Evolution of the Archean Crust of  
638 the São Francisco Craton. pp. 29–56.

639 Thorpe, R.I., Cumming, G.L., Krstic, D., 1984. Lead Isotope Evidence Regarding Age of Gold  
640 Deposits In The Nova Lima District, Minas Gerais, Brazil. *Rev. Bras. Geociências* 14, 147–152.

641 Tomkins, A.G., Frost, B.R., Pattison, D.R.M., 2006. Arsenopyrite melting during metamorphism  
642 of sulfide ore deposits. *Can. Mineral.* 44, 1045–1062.

643 Tomkins, A.G., Pattison, D.R.M., Frost, B.R., 2007. On the initiation of metamorphic sulfide  
644 anatexis. *J.Petrol.* 48, 511–535.

645 Vermeesch, P. (2018). IsoplotR: A free and open toolbox for geochronology. *Geoscience*  
646 *Frontiers*, 9 (5), 1479–1493.

647 Vial, D.S., Abreu, G.C., Schubert, G., Ribeiro-Rodrigues, L.C. 2007. Smaller gold deposits in the  
648 Archean Rio das Velhas greenstone belt, Quadrilátero Ferrífero, Brazil. *Ore Geology Reviews* 32,  
649 651-673.

## 650 **Figure Captions**

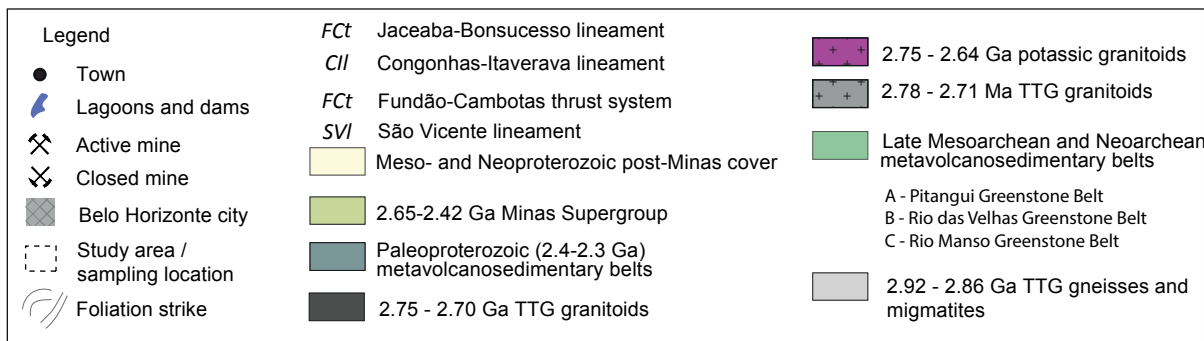
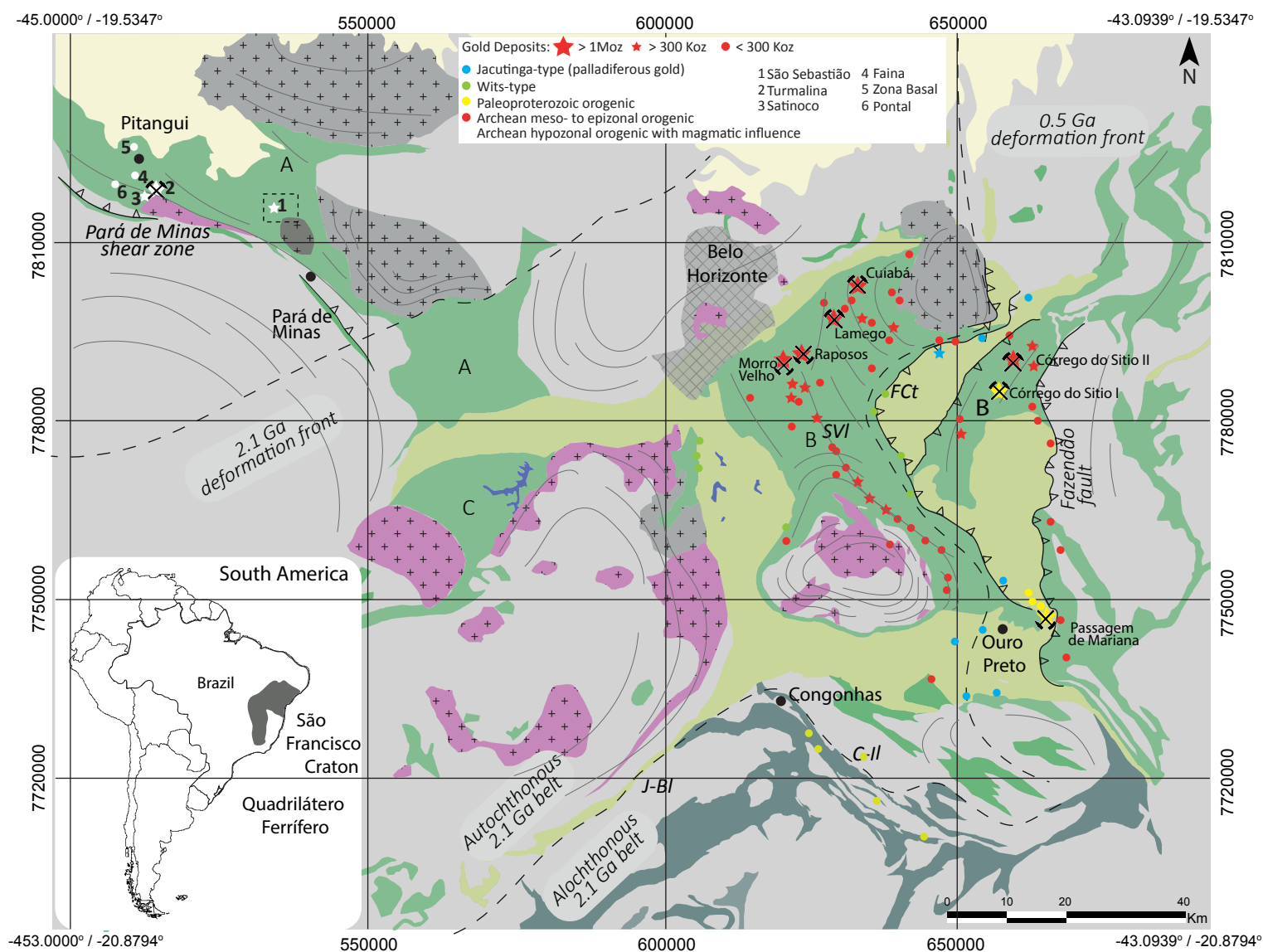
651  
652 **Figure 1:** Regional geological setting of the Quadrilátero Ferrífero in the south sector of the São  
653 Francisco Craton. Map shows the location of São Sebastião (study area marked by dashed  
654 rectangle) and other hypozonal gold deposits in the Pitangui greenstone belt, as well as the  
655 main gold deposits of various types within the Rio das Velhas greenstone belt. Latitude/longitude  
656 geographic coordinates at the corners of the map and UTM in other  
657 intersections. Modified from Dorr (1969), Corrêa Neto et al. (2012), Pinto and Silva (2014), and  
658 Aguilar et al. (2017).

659  
660 **Figure 2:** (A) Transect from a 3D model of the São Sebastião deposit showing the positioning of  
661 drill cores and respective lithological correlation. Modified from the São Sebastião 43101 report  
662 provided by IAMGOLD Brazil (Mitrofanov and Cole, 2020). (B) to (E) Drill core images from  
663 sulfide-rich banded iron formation (BIF) illustrating the various sulfidation stages at São  
664 Sebastião (check Fig. 2J for relative timing). (B) assemblage I pyrrhotite and chalcopyrite ( $po_1 +$   
665  $ccp_1$ ) parallel to the  $S_n$  foliation overgrown by arsenopyrite (apy – assemblage II) preferably  
666 within organic-matter-rich (darker) microbands. Assemblage III pyrrhotite, chalcopyrite ( $po_2 +$   
667  $ccp_2$ ) and pyrite ( $py_1$ ) are late and overgrow previous phases. (C) Coarse-grained arsenopyrite  
668 (coarse apy - assemblage II) overgrowing  $po_1+ccp_1$ . Fine-grained arsenopyrite (fine-apy -

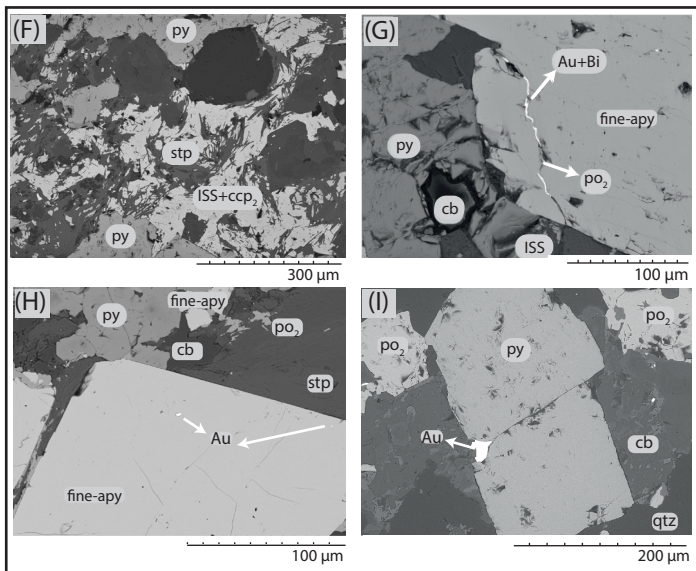
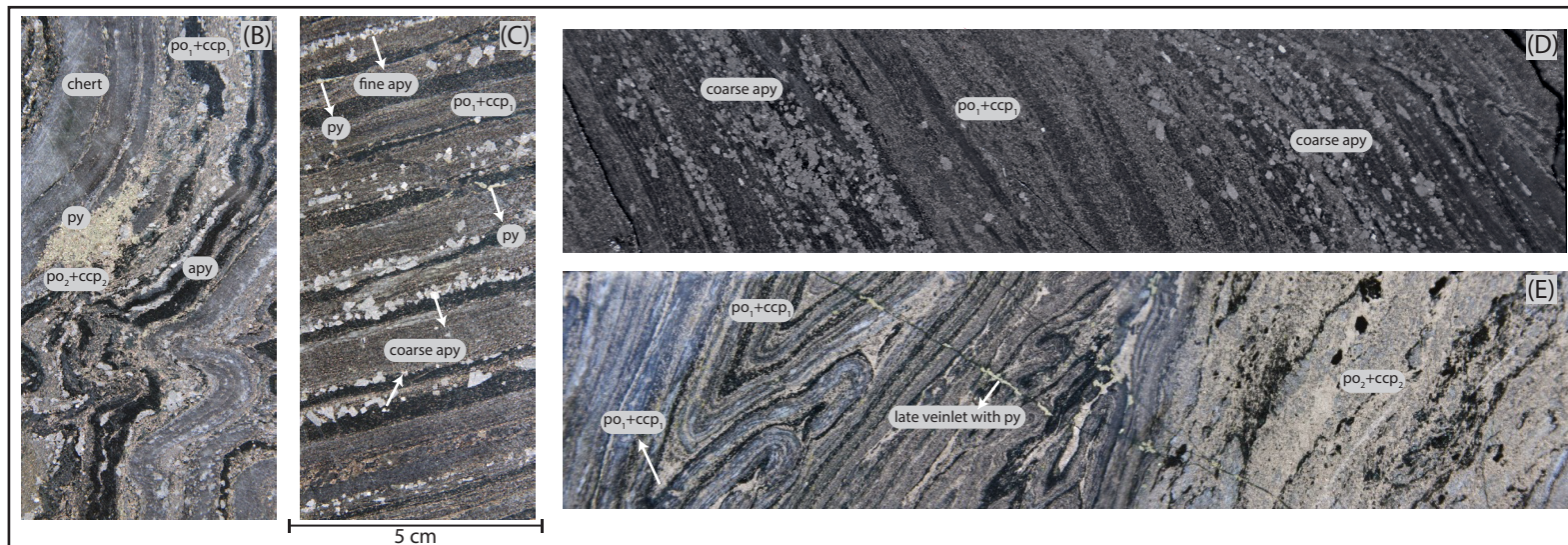
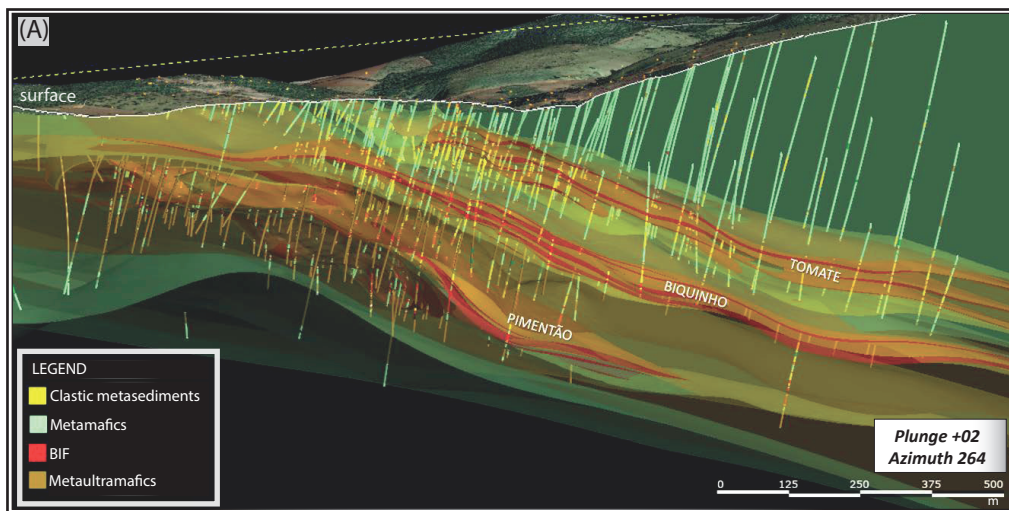
669 assemblage III) occurs in microbands close to pyrite<sub>1</sub> pockets. (D) Sulfide-rich BIF with po<sub>1</sub>+ccp<sub>1</sub>  
1 670 (assemblage I) overgrown by coarse-grained arsenopyrite (assemblage II). (E) Early po<sub>1</sub>+ccp<sub>1</sub>  
2 671 (assemblage I) preferably grown in fold-hinges and small-scale shear zones overgrown by  
3 672 brighter-colored po<sub>2</sub>+ccp<sub>2</sub> (assemblage II), all phases are crosscut by a late veinlet containing  
4 673 pyrite<sub>2</sub>. (F) to (I) SEM images of thin sections from the Biquinho orebody. (F) ISS +  
5 674 ccp<sub>2</sub>+stilpnomelane (stp)+pyrite association. (G) pyrite and ISS at the borders of fine-grained  
6 675 apy with fracture filled by native gold (Au), native bismuth (Bi) and po<sub>2</sub>. (H) Gold inclusions in  
7 676 fine-grained arsenopyrite surrounded by pyrite, po<sub>2</sub>, stilpnomelane and carbonate (cb). (I) Gold  
8 677 associated with pyrite bordered by quartz (qtz), po<sub>2</sub> and carbonate (cb). (J) Paragenetic table  
9 678 showing relative timing of disseminated sulfide assemblages (I, II and III) and late veins – refer  
10 679 to this table for relative timing and assemblage correlation. As-py – arsenian pyrite; sph –  
11 680 sphalerite; Bi-sul – bismuth-sulfosalts; Bi-Te – bismuth tellurides.  
12  
13  
14  
15  
16  
17  
18

19 681  
20 682 **Figure 3:** <sup>187</sup>Re/<sup>188</sup>Os vs. <sup>187</sup>Os/<sup>188</sup>Os isochron plots: (A) for assemblage I pyrrhotite, and  
21 683 assemblage II and III arsenopyrite and pyrite; (B) for assemblage I pyrrhotite; (C) assemblage II  
22 684 arsenopyrite, (D) assemblage III arsenopyrite + pyrite, and (e) <sup>187</sup>Re-<sup>187</sup>Os<sup>r</sup> isochron for  
23 685 assemblage III sulfides. See text for discussion.  
24  
25  
26  
27  
28  
29  
30  
31  
32  
33  
34  
35  
36  
37  
38  
39  
40  
41  
42  
43  
44  
45  
46  
47  
48  
49  
50  
51  
52  
53  
54  
55  
56  
57  
58  
59  
60  
61  
62  
63  
64  
65

Figure 1\_2 columns







		syn to post-D <sub>n</sub> and D <sub>ns1</sub> (Archean)		late high-T paragenesis	late veinlets	
Sulfide assemblages	I	Ore-related phases po <sub>1</sub> ccp <sub>1</sub>	Associated gangue biotite chlorite prismatic Ti-magnetite quartz carbonate	Texture . disseminated // S <sub>n</sub> . filling saddle-reefs and fold hinges in BIF		
	II	As-py coarse-apy	tourmaline grunerite hornblende, Fe-rich garnet	. disseminated, overgrowing S <sub>n</sub>		
	III	fine-apy ISS sph py <sub>1</sub> Bi-sul/ Bi-Te po <sub>2</sub> ccp <sub>2</sub> Au+Bi	stilpnomelane scheelite fluorapatite monazite anhedral Ti-magnetite coarse quartz carbonate	. growing over pyrrhotite, and chalcopyrite, . filling embayments and fractures in previous phases - - - - - inclusions in previous sulfide phases, . disseminated in irregular patches, . disseminated in between the gangue, . filling fractures in apy(both) and py,		
		py <sub>2</sub> ccp <sub>3</sub>	grunerite quartz carbonate	. late veins and veinlets		
Time →						

(J)

Figure 3\_2 columns

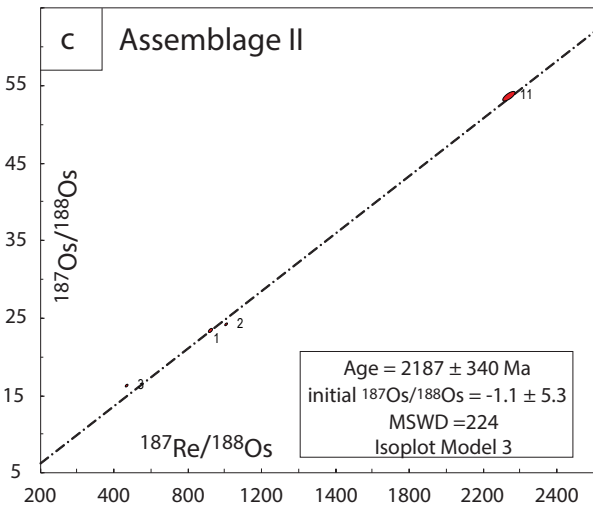
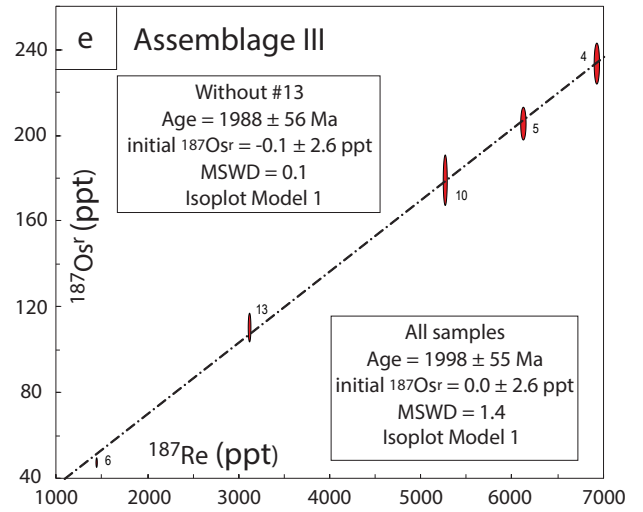
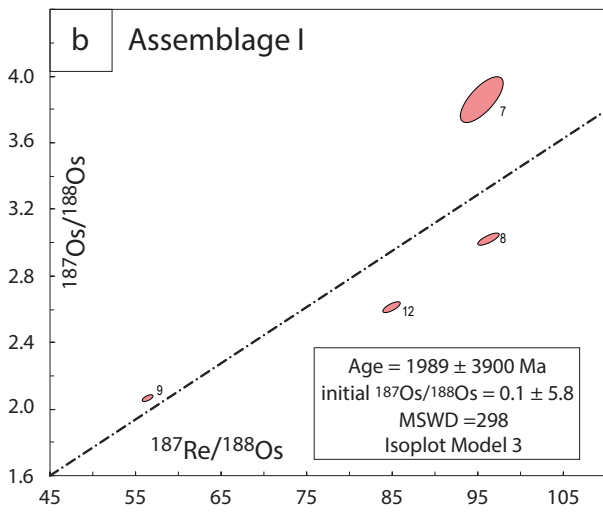
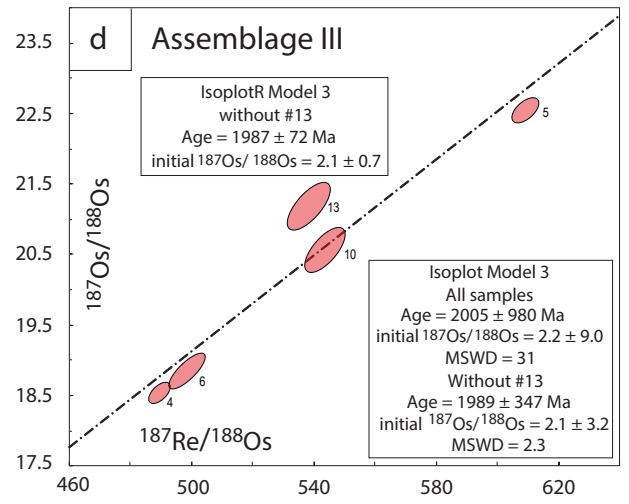
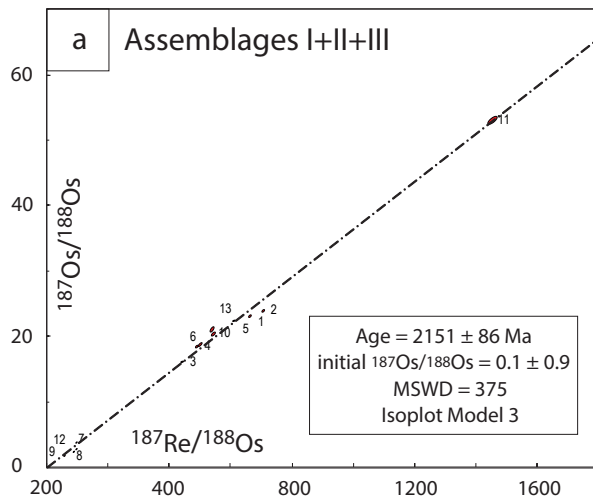


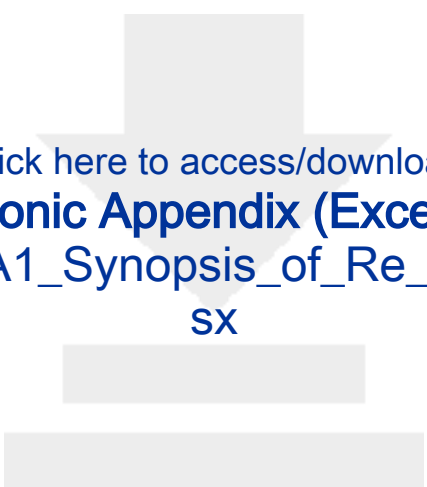
**Table 1.** Synopsis of the Re-Os data for assemblage I, II, and III sulfides.

Name	Batch #	sample #	mineral	Grain size	Assemblage
RO1029-7_CCP1	RO1029-7	7	Pyrrhotite	fine	I
RO1108-2_2Po	RO1108-2	8	Pyrrhotite	fine	I
RO1108-3_3Po	RO1108-3	9	Pyrrhotite	fine	I
RO1108-7_7Po	RO1108-7	12	Pyrrhotite	fine	I
RO1029-1_APY1	RO1029-1	1	Arsenopyrite	coarse	II
RO1029-2_APY2	RO1029-2	2	Arsenopyrite	coarse	II
RO1029-3_APY3	RO1029-3	3	Arsenopyrite	coarse	II
RO1108-5_5Aspy	RO1108-5	11	Arsenopyrite	coarse	II
RO1029-4_APY4	RO1029-4	4	Arsenopyrite	fine	III
RO1029-5_APY+PY	RO1029-5	5	Arsenopyrite+pyrite	fine	III
RO1029-6_PY	RO1029-6	6	pyrite	coarse-fine	III
RO1108-4_4Aspy+Py	RO1108-4	10	Arsenopyrite+pyrite	fine	III
RO1108-8_Aspy	RO1108-8	13	Arsenopyrite	fine	III

Re (ppb)	±	Total Os (ppt)	±	<sup>187</sup> Re (ppb)	±	<sup>192</sup> Os (ppt)	±	<sup>187</sup> Os <sup>r</sup> (ppt) @ Osi = 0.12	<sup>187</sup> Os <sup>r</sup> (ppt) @ Osi = 0.5	<sup>187</sup> Os <sup>r</sup> (ppt) @ Osi = 1.0
0.984	0.004	73.8	1.0	0.618	0.002	20.5	0.4	24.2	21.8	18.5
0.258	0.001	17.8	0.1	0.162	0.001	5.3	0.0	4.9	4.2	3.4
0.238	0.001	25.5	0.1	0.150	0.001	8.4	0.1	5.2	4.2	2.8
0.264	0.001	19.9	0.1	0.166	0.001	6.2	0.0	4.9	4.1	3.2
13.413	0.047	391.7	2.3	8.431	0.030	40.2	0.2	294.3	289.5	283.1
13.629	0.047	383.5	2.3	8.566	0.030	38.5	0.2	290.3	285.7	279.6
12.281	0.054	415.5	2.2	7.719	0.034	55.3	0.2	281.7	275.1	266.4
7.311	0.025	191.9	2.1	4.595	0.016	10.0	0.1	167.7	166.5	164.9
11.014	0.038	369.1	2.1	6.923	0.024	44.8	0.2	260.8	255.4	248.3
9.713	0.037	301.7	1.8	6.105	0.023	31.7	0.1	224.9	221.1	216.1
2.260	0.008	75.2	0.8	1.421	0.005	9.0	0.1	53.4	52.3	50.9
8.361	0.029	271.9	3.2	5.255	0.018	30.6	0.3	197.9	194.2	189.3
4.944	0.017	165.9	2.0	3.107	0.011	18.3	0.2	121.7	119.5	116.6

$^{187}\text{Os}^r$ (ppt) @ Osi = 2.1	±	% $^{187}\text{Os}^r$ @ Osi = 0.12	% $^{187}\text{Os}^r$ @ Osi = 0.5	% $^{187}\text{Os}^r$ @ Osi = 1.0	% $^{187}\text{Os}^r$ @ Osi = 1.5	% $^{187}\text{Os}^r$ @ Osi = 2.1	$^{187}\text{Re}/^{188}\text{Os}$	±	$^{187}\text{Os}/^{188}\text{Os}$
11.4	2.7	96.7	86.9	74.0	61.1	45.6	95.5	2.1	3.87
1.6	0.7	95.8	83.2	66.8	50.3	30.5	96.3	1.0	3.03
-0.1	1.1	94.0	75.7	51.6	27.5	-1.3	56.4	0.5	2.07
1.0	0.8	95.2	80.7	61.6	42.6	19.8	84.9	0.8	2.62
1.0	8.0	99.5	97.8	95.7	93.5	91.0	663.2	3.8	23.27
269.1	7.8	99.5	97.9	95.8	93.7	91.2	704.3	4.0	23.99
266.2	9.0	99.2	96.9	93.8	90.8	87.1	442.1	2.8	16.26
247.2	5.1	99.8	99.0	98.1	97.2	96.0	1453.5	12.4	53.17
232.8	7.8	99.3	97.3	94.6	91.9	88.7	489.3	2.8	18.55
205.1	6.2	99.4	97.8	95.5	93.3	90.7	608.9	3.7	22.56
47.8	1.8	99.2	97.2	94.6	91.9	88.8	498.5	4.9	18.86
178.7	9.7	99.4	97.6	95.1	92.7	89.8	543.5	5.4	20.58
110.3	5.3	99.4	97.6	95.3	92.9	90.1	538.1	5.6	21.19

$\pm$	rho	% Re blank	% <sup>187</sup> Os blank	% <sup>188</sup> Os blank	Model age @Osi = 0.12	Model age @Osi = 0.5	Model age @Osi = 1.0	Model age @Osi = 1.5	Model age @Osi = 2.1	$\pm$
0.11	0.714	0.58	0.22	4.8	2308.7	2078.5	1774.2	1468.3	1099.2	255.2
0.03	0.767	2.90	0.28	3.7	1784.5	1554.1	1249.6	943.5	574.2	248.5
0.02	0.630	3.15	0.26	2.4	2043.0	1650.8	1130.7	606.0	-29.6	425.9
0.02	0.720	2.82	0.28	3.2	1740.8	1479.4	1133.6	785.8	365.8	282.1
0.15	0.569	0.04	0.02	2.5	2059.6	2026.4	1982.6	1938.8	1886.2	37.3
0.15	0.578	0.04	0.02	2.6	2000.5	1969.2	1927.9	1886.6	1837.1	35.2
0.10	0.504	0.05	0.02	1.8	2151.8	2102.0	2036.4	1970.8	1891.9	54.9
0.51	0.741	0.14	0.01	2.7	2151.7	2136.5	2116.6	2096.7	2072.7	21.6
0.12	0.572	0.05	0.02	2.2	2219.4	2174.5	2115.3	2056.1	1984.9	49.7
0.14	0.568	0.06	0.02	3.1	2171.8	2135.7	2088.1	2040.5	1983.3	40.7
0.21	0.788	0.31	0.13	12.2	2214.6	2170.4	2112.3	2054.2	1984.3	49.7
0.26	0.683	0.19	0.02	1.4	2218.3	2177.8	2124.5	2071.2	2007.2	48.2
0.28	0.701	0.29	0.01	1.0	2305.9	2265.0	2211.3	2157.5	2092.9	49.0



Click here to access/download

**Electronic Appendix (Excel etc.)**

Appendix\_Table\_A1\_Synopsis\_of\_Re\_Os\_data\_FINAL.xl

SX